

# Chapter 9

## LEAP-ASIA-2019 Centrifuge Test at KAIST



Satish Manandhar, Seong-Nam Kim, and Dong-Soo Kim

**Abstract** Since Niigata and Alaska earthquakes in 1964, the dangers of liquefaction are well established, and research into liquefaction has been actively performed. In this context, Liquefaction Experiments and Analysis Projects (LEAP) was launched to provide high-quality experimental data on soil liquefaction using laboratory testing and centrifuge modeling and then validating numerical models to improve predictions. The purpose of LEAP-ASIA-2019, which is one of the LEAP programs, was to fill the gaps and further extend/establish/confirm the trends obtained in the previous LEAP-UCD-2017 program. Further, the validity of the generalized scaling law was also tested for liquefaction simulation using different 1-g and centrifuge scaling factors. During LEAP-ASIA-2019, KAIST performed two model tests (Model A and Model B) with the same target relative density ( $D_r = 85\%$ ) and input motion intensity of 0.3g. Models A and B were identical in construction but were tested under different centrifugal accelerations to verify the generalized scaling factors. This paper describes the experimental procedure in detail and the responses of dense model grounds to strong base shaking in terms of ground accelerations, excess pore pressure, surface displacements, stress-strain behavior, and CPT profiles. Further, discussion on the generalized scaling law and the effect of shaking history on the model behavior are also presented.

**Keywords** Liquefaction Experiments and Analysis Projects (LEAP-ASIA-2019) · Generalized scaling law (GSL) · Centrifuge modeling

### 9.1 Introduction

Liquefaction is a phenomenon in which the strength and stiffness of saturated soil are reduced because of the reduction in effective confining stress during earthquakes. Damage and ground failure due to liquefaction remain a major concern to

---

S. Manandhar · S.-N. Kim (✉) · D.-S. Kim  
Department of Civil and Environmental Engineering, Korean Advanced Institute of Science and Technology, KAIST, Daejeon, Republic of Korea  
e-mail: [seong8nam@kaist.ac.kr](mailto:seong8nam@kaist.ac.kr)

© The Author(s) 2024  
T. Tobita et al. (eds.), *Model Tests and Numerical Simulations of Liquefaction and Lateral Spreading II*, [https://doi.org/10.1007/978-3-031-48821-4\\_9](https://doi.org/10.1007/978-3-031-48821-4_9)

geotechnical engineers. Various methods such as field investigation and laboratory tests have been conducted to evaluate the triggering phenomenon and consequences of liquefaction. Simultaneously, studies involving numerical simulations have produced different insights into liquefaction.

Numerical modeling is a cost-effective way to evaluate the consequences of liquefaction on built structures. However, the constitutive models and numerical analysis techniques that simulate complex liquefaction phenomena must be validated using well-defined experimental results (Ueda & Iai, 2018). Under such a demand, a collaborative study between numerical modelers and centrifuge experimenters was conducted 20 years ago, termed VELACS (Arulanandan & Scott, 1993). Similar to VELACS, Liquefaction Experiments and Analysis Projects (LEAP) is an ongoing collaborative project, which aims to reduce the inconsistency in experimental results and thus provide high-quality experimental data for validation of numerical models.

LEAP-GWU-2015 was one of the first validation efforts within the ongoing LEAP program, where six institutions conducted centrifuge tests on liquefaction of a sloping ground in a rigid box (Kutter et al., 2018). The 2015 exercise demonstrated the feasibility of an approach for a next-generation validation database and showed that variations in initial conditions and ground motions led to differences in results between institutions for the same model.

After LEAP-GWU-2015, 9 facilities participated in LEAP-UCD-2017 and performed 24 centrifuge tests to simulate the liquefaction of a submerged sloping sand deposit. The purpose of LEAP-UCD-2017 was to characterize the trend and sensitivity of the model response according to the relative density of the model ground and input motion intensity. The correlations between lateral displacement, relative density based on CPT cone tip resistance, and effective PGA were better than the correlations between lateral displacement, relative density based on volume and mass measurements, and PGA (Kutter et al., 2019). In addition, the accelerations and pore water pressure records at different depths were compared between different institutions.

In line with the LEAP program, LEAP-ASIA-2019 was undertaken to validate the generalized scaling law (Iai et al., 2005) using modeling of model technique and to obtain additional results, which could be used to fill the gaps and further extend/establish/confirm the trends obtained in the LEAP-UCD-2017. The generalized scaling law is needed to overcome size restrictions while testing large prototypes by combining the 1-g scaling law with the centrifuge scaling law (Garnier et al., 2007). The same nine institutions who participated in the LEAP-UCD-2017 also participated in the LEAP-ASIA-2019 round-robin centrifuge tests.

KAIST developed a geotechnical centrifuge facility with a centrifuge of 5 m radius and 240g-ton capacity in 2009 and participated in LEAP-UCD-2017 (Kim et al., 2020) and LEAP-ASIA-2019. Following the specifications of LEAP-ASIA-2019, KAIST performed two centrifuge model tests (Model A and Model B) with the same soil relative density ( $D_r = 85\%$ ) and target input motion intensity of 0.3g. Models A and B are identical with LEAP-UCD-2017 in construction, but the

viscosity of pore fluid and the centrifugal accelerations were scaled based on the generalized scaling law for Model B. This paper provides details of the centrifuge model tests conducted at KAIST for LEAP-ASIA-2019, including facility and equipment, test procedure, and results.

## 9.2 Generalized Scaling Law and Overview of Experimental Condition

Centrifuge model testing can be beneficial to test small-scaled models at higher  $g$ -levels, so that the stress distribution is similar with the prototype condition. However, for large prototype structures, the scaled model could still be large enough for testing due to centrifuge limitations, such as the size of the model container and scaling effects on materials. To resolve the demand for large-scale prototype testing and restrictions on centrifuge modeling, Iai et al. (2005) proposed the generalized scaling law by combining the scaling law for centrifuge testing and one for 1-g dynamic model testing. This is called the “generalized scaling law” in dynamic centrifuge modeling.

The main concept of the generalized scaling law is to scale the prototype twice resulting in much larger overall scaling factor, which would result in a reasonable sized centrifuge model suitable for testing. First, the prototype is scaled down via a similitude for 1-g shaking table tests to a virtual 1-g model. The virtual 1-g model is subsequently scaled down by applying a similitude for centrifuge tests to the actual physical model. Figure 9.1 visualizes the concept of the generalized scaling law using virtual 1-g models. In this way, the geometric scaling factors applied in 1-g tests ( $\mu$ ) can be multiplied with those for centrifuge tests ( $\eta$ ) resulting in much larger overall scaling factor  $\lambda = \mu\eta$ . The generalized scaling factors are given in Table 9.1 along with scale factors for centrifuge and 1-g tests.

The generalized scaling law can be validated using modeling of model technique. Two centrifuge models (Models A and B) made with the same overall scaling factors ( $\lambda = 40$ ) but different 1-g scale factor ( $\mu = 1$  for Model A and  $\mu = 1.5$  for Model B) and centrifuge scaling factor ( $\eta = 40$  for Model A and  $\eta = 26.7$  for Model B) can be compared with each other. These scaling factors were the ones implemented in KAIST centrifuge experiments. Model A represents conventional centrifuge scaling factors, while Model B represents the generalized scaling factors. Different scaling factors were assigned to different institutions in LEAP-ASIA-2019 for verifying the generalized scaling law. The scale factors for different physical parameters for KAIST Models A and B are given in Table 9.1.

Figure 9.2 shows the relative densities of the ground model and the intensity of the input base motions for the various tests during the LEAP-UCD-2017 program. The red circle zone is the experimental condition of LEAP-ASIA-2019, and the red star is the experimental condition for KAIST. One of the purposes in LEAP-ASIA-2019 was to evaluate the occurrence of liquefaction under the application of

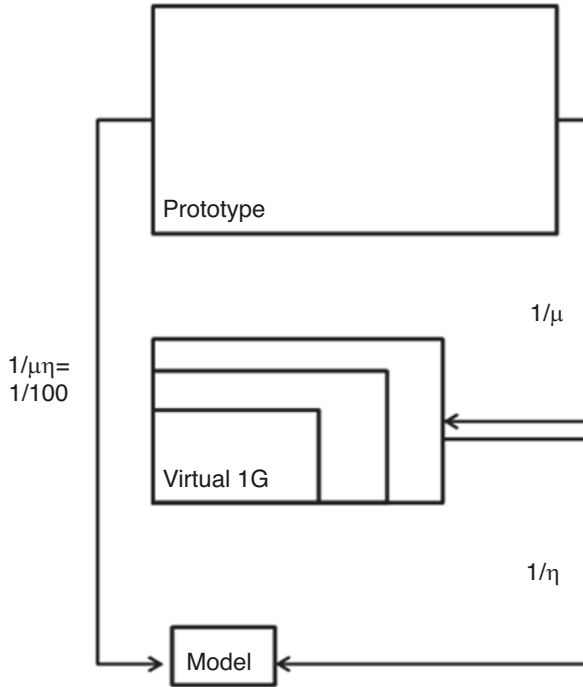


**Fig. 9.1** Principle of the generalized scaling law. (Tobita & Iai, 2011)

**Table 9.1** Scaling factors for KAIST Models A and B based on conventional centrifuge scaling factors and generalized scaling factors for various physical parameters

	(1) Scaling factors for 1-g test	(2) Conventional centrifuge scaling factors	(3) Generalized scaling factors	Model A Conventional centrifuge scaling factors ( $\mu = 1, \eta = 40$ )	Model B Generalized scaling factors ( $\mu = 1.5, \eta = 26.7$ )
Length	$\mu$	$\eta$	$\mu\eta$	40.000	40.000
Density	1	1	1	1.000	1.000
Time	$\mu^{0.75}$	$\eta$	$\mu^{0.75}\eta$	40.000	36.189
Frequency	$\mu^{-0.75}$	$1/\eta$	$\mu^{-0.75}/\eta$	0.025	0.028
Acceleration	1	$1/\eta$	$1/\eta$	0.025	0.037
Velocity	$\mu^{0.75}$	1	$\mu^{0.75}$	1.000	1.355
Displacement	$\mu^{1.5}$	$\eta$	$\mu^{1.5}\eta$	40.000	49.051
Stress	$\mu$	1	$\mu$	1.000	1.500
Strain	$\mu^{0.5}$	1	$\mu^{0.5}$	1.000	1.225
Stiffness	$\mu^{0.5}$	1	$\mu^{0.5}$	1.000	1.225
Permeability	$\mu^{0.75}$	$\eta$	$\mu^{0.75}\eta$	40.000	36.189
Pore pressure	$\mu$	1	$\mu$	1.000	1.500
Tip resistance	$\mu$	1	$\mu$	1.000	1.500

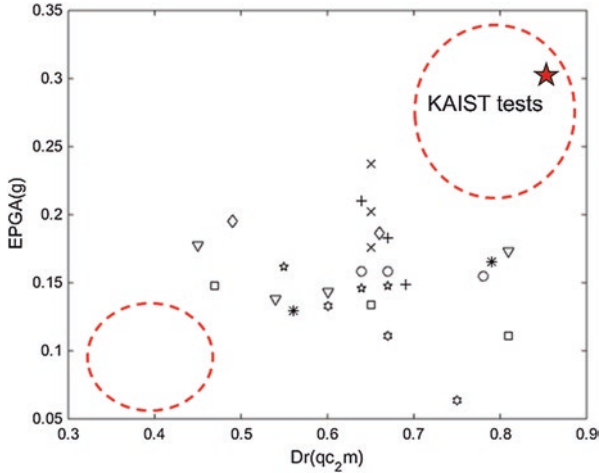


**Fig. 9.2** Effective peak ground acceleration (EPGA) versus relative density ( $D_r$ ) from cone tip resistance at 2 m depth ( $q_{c2}$ ) for various test models in LEAP-UCD-2017 experiments. The red circles represent the experimental conditions for LEAP-ASIA-2019. Red star is the experimental condition for KAIST tests

strong base shaking on dense model grounds and weak base shaking on loose model grounds. The target experimental condition at KAIST is to evaluate liquefaction behavior by applying strong base motion of 0.3g intensity to the ground model of 85% relative density. The other purpose of LEAP-ASIA-2019 is to validate the applicability of the generalized scaling law in liquefaction simulation by comparing the results of Model A and Model B.

### 9.3 Centrifuge Model Construction

#### 9.3.1 Centrifuge Facility at KAIST

KAIST has a geotechnical centrifuge facility housing an automatic balancing beam centrifuge with a platform radius of 5 m and maximum capacity of 240g-tons (Kim et al., 2013a). Target input motions were applied using an earthquake simulator that uses a dynamic self-balancing technique to eliminate a large portion of the undesired reaction forces and vibrations transmitted to the main body (Kim et al., 2013b). The geotechnical centrifuge along with the shaking table used in KAIST centrifuge tests is shown in Fig. 9.3. The centrifuge tests in KAIST were conducted at a centrifugal acceleration of 40g for Model A and 26.67g for Model B. From now on, all measurements are in prototype scale, unless explicitly stated.

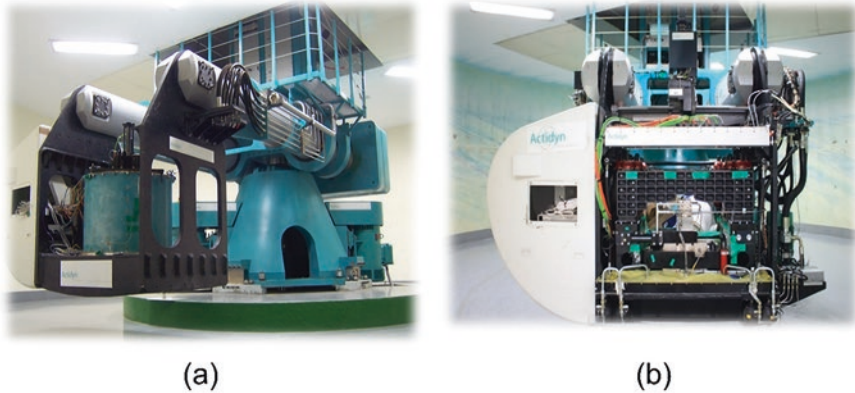


**Fig. 9.3** Geotechnical centrifuge facility at KAIST: (a) centrifuge main body and (b) earthquake simulator

### 9.3.2 Soil Material and Density

Ottawa F-65 sand was used as the standard sand for LEAP-ASIA-2019. The grain size characteristics and property of the soil are as follows:  $G_s = 2.665$ ,  $D_{10} = 0.13$  mm,  $D_{30} = 0.17$  mm,  $D_{50} = 0.20$  mm, and  $D_{60} = 0.21$  mm (El Ghoraiby et al., 2020). Based on the specifications for LEAP-ASIA-2019, the minimum and maximum densities of sand were determined as  $\rho_{dmax} = 1757$  kg/m<sup>3</sup> and  $\rho_{dmin} = 1490.5$  kg/m<sup>3</sup>, respectively. The target soil density for Models A and B in KAIST was specified as 1711 kg/m<sup>3</sup>, equivalent to 85% relative density.

The sand model was constructed by dry pluviation through a sieve with an opening size of approximately 1.20 mm; the sieve was partially blocked to limit the flow. The density of the soil model was determined by the size of the opening slot and the drop height, for which calibration tests were done. Figure 9.4 shows the geometry of the opening slots and the calibration test results for soil density and pluviation drop heights, along with the required drop height for constructing the dense soil models.

The measured dry unit weights of the model grounds constructed in a rigid box were 1716.55 kg/m<sup>3</sup> and 1720.6 kg/m<sup>3</sup> for Models A and B, respectively, based on mass and volume measurements. After the sand was pluviated to the target height, a 5° inclined guide was installed on the top of the model box. A manufactured scraper was connected directly to the inclined guide and was used to scrap the soil surface carefully. The soil generated by the scraping was removed carefully by using a vacuum cleaner so that the resulting ground was not disturbed, and a 5° sloped model ground was achieved.

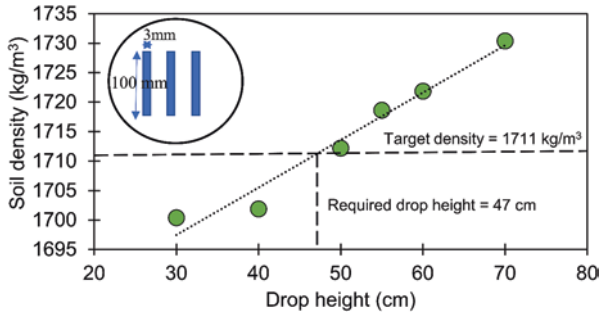


**Fig. 9.4** Density versus drop height relationship for the sieve design and the required drop height to achieve model of target density

### 9.3.3 Viscous Fluid

The viscous fluid was a mixture of water and methylcellulose, and the target viscosity was set to 40 cSt for Model A as dictated by the centrifuge scaling law and 36.1 cSt for Model B based on the generalized scaling law. Temperature and concentration are the influencing factors of fluid viscosity; thus, calibration tests are needed before making the viscous fluid. The viscosity was measured using a Brookfield-type automatic viscometer. The automatic viscometer relates frictional resistance to viscosity by rotating a spindle inside the fluid as shown in Fig. 9.5. In addition, a temperature sensor measures the fluid temperature at the current viscosity.

The results of the calibration tests are shown in Fig. 9.6. For a given concentration, the viscosity increases with a decrease in temperature, while for a given temperature, the viscosity increases with an increase in concentration of methylcellulose. Based on the calibration results, the concentrations of methylcellulose were 2.08% (case #4) and 2.0% (case #3) at 18 °C for 40 cSt and 36.1 cSt target viscosities, respectively. Upon preparing the viscous fluid, the achieved viscosities of the fluid used in Models A and B were 41.3 cSt and 36.2 cSt, respectively, which is close to the target viscosities.

### 9.3.4 Model Description and Instrumentations

The model construction is identical with LEAP-UCD-2017, which consists of a 5° sloping sand ground model in a rigid box. The rigid box has an internal dimension of 570 mm × 225 mm × 450 mm (length × width × depth) in the model scale with a front transparent window. The model ground constructed through dry pluviation is described in Fig. 9.7, with the following dimensions in the prototype scale: 22.8 m × 4 m × 9 m (length × depth at midpoint × width). The length of the slope (22.8 m) was about 15% greater than the specified length (20 m). In the KAIST centrifuge facility, the 5° inclination along the length of the model was not curved

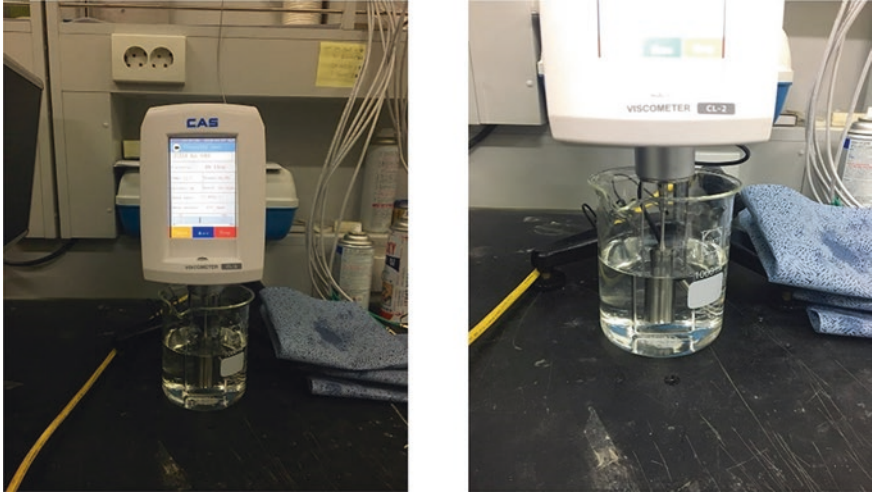


Fig. 9.5 Brookfield-type automatic viscometer used in calibration tests of viscous fluid

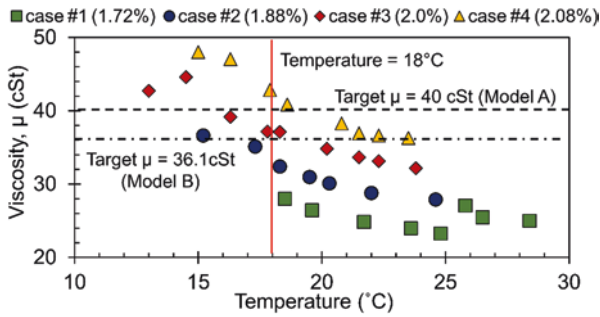


Fig. 9.6 Calibration tests for viscosity according to temperature and concentration using automatic viscometer

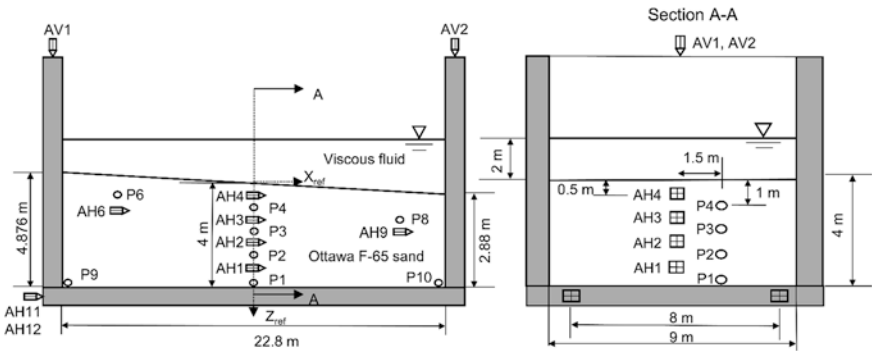


Fig. 9.7 Schematic of KAIST centrifuge test model and instrumentation



**Table 9.2** Detailed information of instrumentations used in KAIST experiments

Instrument	Type	Name	Description
Accelerometer	353B17	AH1–AH4, AH6, AH9	Soil horizontal acceleration
		AH11–AH12	Box horizontal acceleration
		AV1–AV2	Box vertical acceleration
Pore pressure transducer	PDCR 81	P1–P4, P6, P8	Pore water pressure in soil
	EPB-PW-3.5BS-V5/L5M	P9–P10	Pore water pressure at the bottom boundary

because the shaking plane was perpendicular to the plane of rotation of the centrifuge, and the centrifuge arm was big enough to mitigate the effect of ground curvature.

The responses of the soil model during shaking were monitored using eight accelerometers along the direction of shaking (AH1–AH4 in the center soil, AH6 and AH9 in the soil close to container boundary, and AH11–AH12 on the rigid container), two vertical accelerometers (AV1 and AV2), and eight pore pressure transducers (P1–P4 in the center of soil model, P6 and P8 in the soil close to side boundary, and P9–P10 at the bottom boundary). The instrument layout is shown in Fig. 9.7. Table 9.2 lists the details of the instrumentation used.

The required 18 surface markers were installed on the ground uniformly with a spacing of 2 m × 2 m. The markers, with a diameter of 26 mm (model scale), were manufactured using PVC material and were designed to be anchored to the soil surface and provide a minimal restriction to pore pressure drainage. A high-speed camera was mounted on the centrifuge arm to measure the plan view lateral displacements of the surface markers during shaking. The high-speed camera at KAIST is a Phantom v5.1 HI-G, which can record videos at 1200 frames per second at a resolution of 1024 × 1024 pixels. The self-balanced system of the shaking table and the hinges connecting the basket to the centrifuge arm isolate the camera from vibrations.

### 9.3.5 Saturation System at KAIST

Figure 9.8 shows the schematic of the saturation system at KAIST. Before saturating, the box was confirmed to be completely sealed from external air. The procedure for the saturation process is as follows: vacuum pressure (−95 kPa) was applied and then a low-pressure CO<sub>2</sub> (15 kPa) was flooded in the box repeatedly. This process was performed five times. In addition, a strong vacuum pressure was also applied to eliminate the trapped air in the viscous fluid container. While maintaining the same vacuum pressure in the rigid box and viscous fluid container, the viscous fluid was slowly dripped into the ground model. The dripping point was in the downslope direction, and to minimize the impact of falling fluid on the soil surface, a sponge

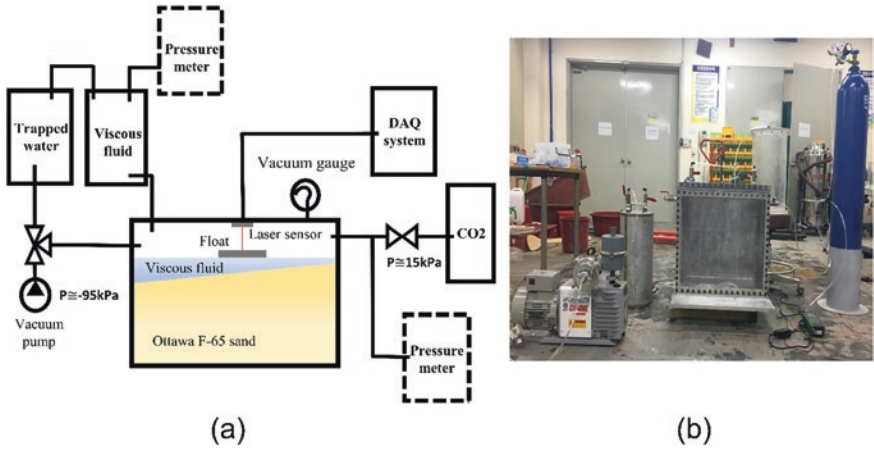


**Fig. 9.8** Saturation system used in KAIST. (a) Schematic of saturation system. (b) Actual saturation system

**Table 9.3** Summary of model parameters for Model A and Model B

Parameters	Model A (Conventional scaling law)	Model B (Generalized scaling law)
Density via mass and vol. measurements ( $\text{kg/m}^3$ )	1716.5	1720.6
Relative density (%)	87	88
Viscosity (cSt)	41.3	36.2
Degree of saturation (%)	99.93	99.94

was installed at the point of impact. After the fluid depth was 5 cm (in model scale) higher than the soil surface, Okamura’s method was used to measure the degree of saturation (Okamura & Inoue, 2012). The degree of saturation measured was 99.93% and 99.94% for Models A and B, respectively, indicating full saturation. Table 9.3 shows the summary of model parameters for Models A and B.

### 9.3.6 Sequence of the Centrifuge Test

Table 9.4 summarizes the typical sequence of the centrifuge tests. In each of the centrifuge tests, four seismic excitations were applied: two low-intensity non-destructive motions and two high-intensity destructive motions. The frequency wavelets covering a wide range were used as a non-destructive motion for ground identification before and after liquefaction. A tapered sine wave with a frequency of 1 Hz was used as the destructive wave. In the KAIST centrifuge tests, the target effective PGA was specified as 0.3g for both the first (Motion #2) and the second

**Table 9.4** Major events in centrifuge test sequence for Models A and B

Event	g-level (Model A/B)	Event description
Event #1 (CPT)	40g/26.7g	CPT (before motion #2)
Event #2 (seismic excitations)	40g/26.7g	Motion #1 and motion #2 (target: 0.3g)
Event #3(CPT)	40g/26.7g	CPT (after motion #2)
Event #4 (seismic excitations)	40g/26.7g	Motion #3 (target: 0.3g) and motion #4

(Motion #3) destructive motions. By applying the destructive motions of the same intensity, the pre- and post-liquefaction behavior can be compared.

Cone penetration tests were also conducted before and after the first destructive motion (Motion #2) to evaluate the soil condition. All facilities participating in LEAP used the same cone design with a cone tip diameter of 6 mm (Carey et al., 2020). The penetration velocity was slow at 2.5 and 3.74 mm/s (model scale) for Models A and B, respectively, and the penetration depth was more than 75 mm (model scale). The CPTs were conducted at locations selected to avoid the sensors installed in the ground model and the markers on the ground surface. As it was necessary to install guide rack and loading actuator above the model box for the CPT, the centrifuge was stopped and restarted to remove the CPT system during seismic excitations. When the centrifuge stopped, the positions of the surface markers were also investigated.

Residual pore pressures (RPPA) were also recorded before and after every major event and change in centrifuge g-level. Recording of RPPA was done while the centrifuge speed was stable and excess pore pressures were 99.9% dissipated.

## 9.4 Test Results

### 9.4.1 Achieved Input Motions

The earthquake simulators of most facilities generate various amounts of high-frequency components, which were superimposed on the smooth ramped sine wave motion. Therefore, effective PGA ( $PGA_{eff}$ ) concept was introduced to compare the results among the facilities that generated different amounts of high-frequency content in the input motion. The  $PGA_{eff}$  can be calculated by Eq. 9.1.

$$PGA_{eff} = PGA_{1Hz} + 0.5 \times PGA_{hf} \tag{9.1}$$

where  $PGA_{1Hz}$  is the PGA of the isolated 1 Hz input signal and  $PGA_{hf}$  is the peak acceleration of the high-frequency components of the input motion (Kutter et al., 2018).

Figure 9.9 shows the main destructive motions (Motions #2 and #3) applied to each model along with the isolated high-frequency noise and the 1 Hz component. A notched band-pass filter with corner frequencies of 0.8 Hz and 1.2 Hz was used

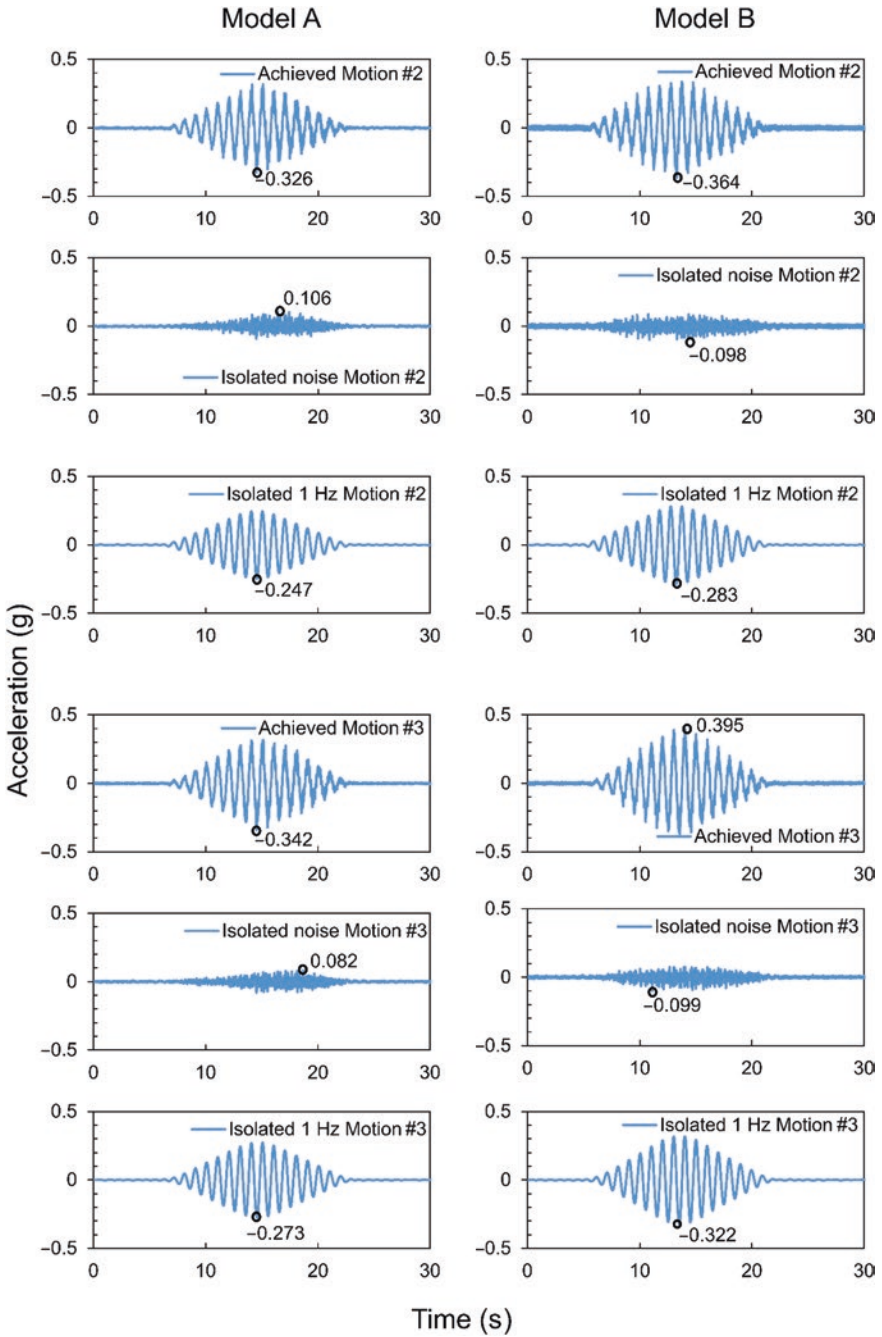


**Fig. 9.9** Time series of the achieved base motion, isolated noise, and isolated 1 Hz signal of Motions #2 and #3 along with peak values in Models A and B

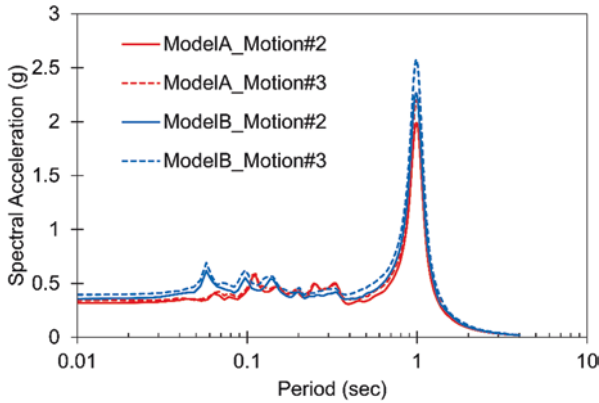


**Fig. 9.10** Response spectra of the achieved base motions (Motions #2 and #3) for Models A and B (5% damping)

to obtain these results. Corresponding peak values in each plot are also shown. The achieved base motion is the raw motion recorded by AH11 and AH12 accelerometers attached to the base of the model box; the achieved base motion shown here is the average of AH11 and AH12.

The acceleration response spectra of the achieved base motions as presented in Fig. 9.10 show that the input motions contain some high-frequency components. However, compared to the achieved base motions of other facilities participating in LEAP-UCD-2017 and LEAP-ASIA-2019, the high-frequency components are smaller, and input motions similar to the target were achieved for KAIST model tests.

Table 9.5 lists the details of all the applied motions. Motions #1 and #4 are non-destructive motions with weak intensity for system identification. The  $PGA_{eff}$  of the input motions applied in these tests were slightly higher than the target  $PGA_{eff}$  (i.e., 0.3g) for Motions #2 and #3 of Model A and Motion #2 of Model B. However, for Motion #3 of Model B, the difference between target and achieved  $PGA_{eff}$  is large. Although the intensity of the destructive motions applied to each model is somewhat larger than the target intensity, it is reasonable for evaluating the liquefaction behavior of dense models during strong shaking, because it aligns with the objective of LEAP-ASIA-2019.

Upon comparing the  $PGA_{eff}$  for Models A and B, the destructive input motions (Motions #2 and #3) for Model B were slightly larger than that for Model A. The difference between  $PGA_{eff}$  of Models A and B was bigger in the case of Motion #3 than Motion #2. Nevertheless, the achieved base motions can be considered similar for Models A and B.

**Table 9.5** Details of various motions applied to Models A and B

		Target $PGA_{\text{eff}}$ (g)	$PGA_{\text{raw}}^a$ (g)	$PGA_{\text{eff}}$ (g)	$PGA_{\text{hf}}$ (g)	$PGA_{1\text{Hz}}$ (g)
Model A ( $\mu = 1, \eta = 40$ )	Motion #1	0.015	0.052	0.044	0.021	0.033
	Motion #2	0.30	0.326	0.300	0.106	0.247
	Motion #3	0.30	0.342	0.314	0.082	0.273
	Motion #4	0.015	0.05	0.054	0.028	0.030
Model B ( $\mu = 1.5, \eta = 26.7$ )	Motion #1	0.015	0.088	0.074	0.046	0.051
	Motion #2	0.30	0.364	0.332	0.098	0.283
	Motion #3	0.30	0.395	0.371	0.099	0.322
	Motion #4	0.015	0.077	0.066	0.039	0.046

<sup>a</sup>Peak horizontal acceleration recorded at the container base

### 9.4.2 Cone Penetration Test Results

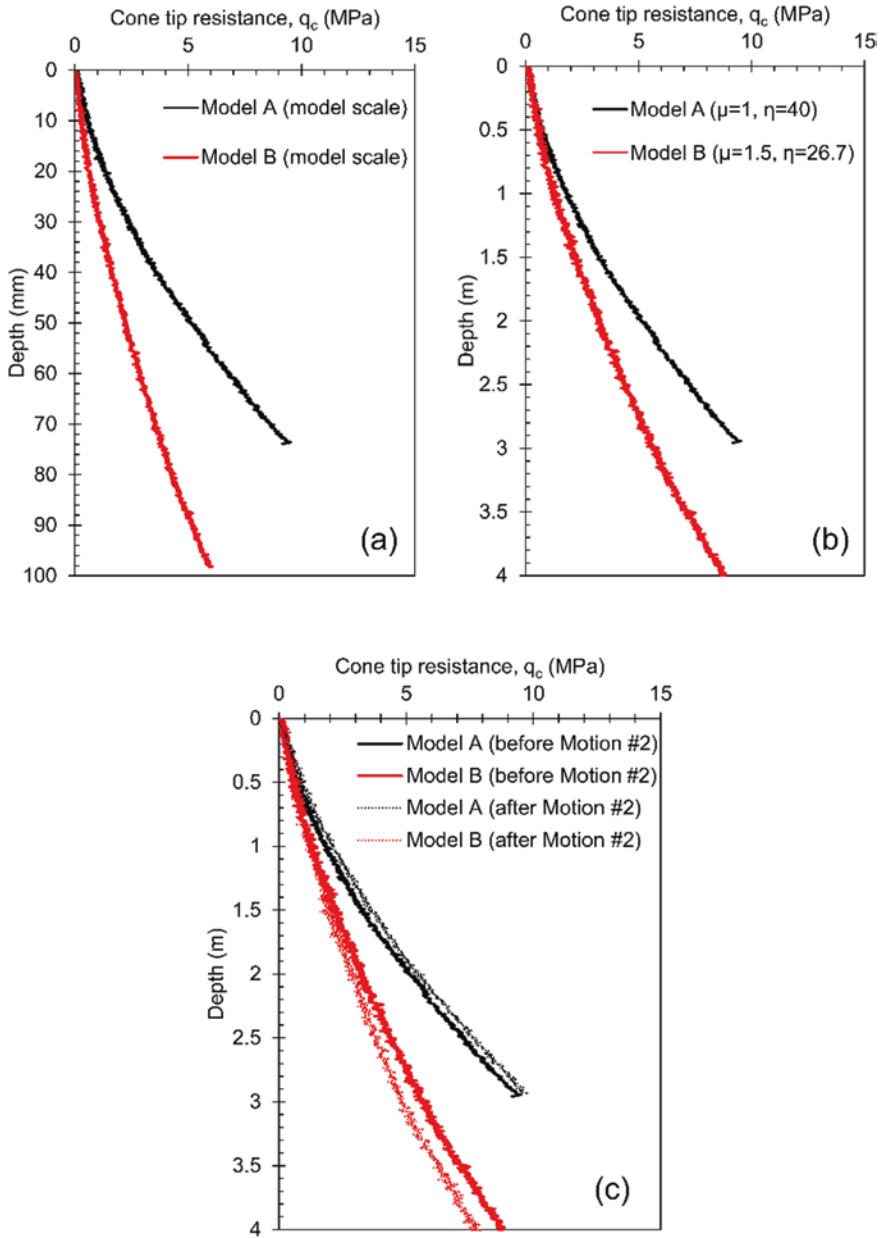
The depth of penetration and the cone tip resistance ( $q_c$ ) were converted to the prototype scale using the scaling factors for Models A and B as shown in Table 9.1. The length scale factors were used for scaling the penetration depths.

Figure 9.11a, b represents the  $q_c$  with penetration depth at the model and the prototype scales for Models A and B before Motion #2. In the model scale, although Models A and B are similar in construction, the  $q_c$  profiles are very different; the  $q_c$  profile is larger for Model A than for Model B. This is due to larger confining pressure in Model A than in Model B because of the differences in the centrifugal acceleration; Model A was tested at 40g, while Model B was tested at 26.7g. In the prototype scale, the difference in  $q_c$  profiles between Models A and B is reduced. At shallow depths (<1 m), the  $q_c$  profiles of both models are similar, but at deeper depths, Model A shows relatively larger  $q_c$  than Model B. This implies that the generalized scaling law may not be applicable at deeper depths because of the effect of larger confining pressure.

Another possible reason for the difference between  $q_c$  profiles between Models A and B is due to higher CPT penetration rate used for Model B than specified. The penetration rate of CPT should be scaled depending on the pore fluid viscosity ( $\mu^*$ ) based on Eq. 9.2 (Kutter et al., 2020a).

$$V_{\text{cpt}} = (100 \text{ mm / s}) / \mu^* \quad (9.2)$$

where  $\mu^*$  is the pore fluid viscosity and  $V_{\text{cpt}}$  is the penetration velocity of the cone. For Model A ( $\mu^* = 41.2$  cSt),  $V_{\text{cpt}}$  should be 2.42 mm/s, and 2.5 mm/s was adopted. For Model B ( $\mu^* = 36.2$  cSt),  $V_{\text{cpt}}$  should be 2.76 mm/s, but 3.72 mm/s was adopted by mistake. A higher penetration rate could result in partial drainage conditions around the cone tip, which contrasts with the fully drained conditions generally assumed for CPT in sand. As a result, the  $q_c$  values for Model B could be smaller as reduced drainage causes excess pore pressure to increase around the cone tip (Kim et al., 2008). Comparison of the  $q_c$  profiles of dense models from other institutions



**Fig. 9.11** Cone tip resistance ( $q_c$ ) and penetration depth from CPT: (a)  $q_c$  versus depth for Models A and B before Motion #2 (model scale), (b)  $q_c$  versus depth for Models A and B before Motion #2 (prototype scale), and (c)  $q_c$  versus depth for Models A and B before and after Motion #2

under the same 1-g and centrifuge scaling factors should be performed to investigate the effect of higher penetration rate.

Figure 9.11c presents the  $q_c$  value with depth before and after Motion #2 for each model at the prototype scale. The  $q_c$  values were slightly larger after Motion #2 for Model A, while for Model B, it was almost the same at shallow depths (<1.5 m) with slight reduction at deeper depths. In the case of Model A, the increase in  $q_c$  could be due to soil densification because of particle rearrangement or liquefaction-induced reconsolidation. For Model B, the time for dissipation of excess pore pressure is longer due to smaller elastic stiffness under lower centrifugal acceleration (Tobita & Iai, 2011). Also, the time for consolidation of Model B is shorter because it has to reach centrifugal acceleration of 26.7g as opposed to 40g for Model A. Therefore, Model B may not have fully consolidated following Motion #2 resulting in smaller  $q_c$  values at the deeper depths.

### 9.4.3 Comparison of Acceleration Response

The acceleration response of Models A and B was converted to the prototype scale using scaling factors shown in Table 9.1. Figure 9.12 shows the response of the four accelerometers installed at the center of the model ground together with the response spectra and the ratio of response spectra (RRS) during Motion #2. The RRS is calculated based on Eq. (9.3). As seen in Table 9.5, the  $PGA_{\text{eff}}$  for Model B was slightly larger than for Model A. dilation spikes, which are caused by the de-liquefaction shock waves (Kutter & Wilson, 1999), are observed more clearly in the sensors installed near the surface (AH4 and AH3), which indicates that the soil may have liquefied. The dilation spikes are unsymmetrical due to the sloping ground model; the spikes are triggered extensively in the direction of static shear stress (downslope direction). The response spectra for both the models are similar except at the short-period range; Model A showed slightly larger high-frequency acceleration spikes than Model B. This is clearer in Fig. 9.12c, where the RRS is larger for Model A than for Model B at the short-period range. An interesting observation is that the spectral acceleration at the period of 1 s is almost the same at all depths and no amplification occurred for the main frequency component of the base motion.

$$\text{RRS} = \frac{\text{Response spectra of soil motions AH1 AH4}}{\text{Response spectrum of the base motion}} \quad (9.3)$$

Figure 9.13 shows the acceleration time history, the response spectra, and the RRS at different depths in Models A and B during Motion #3. In Model A, the amplitude of the dilation spikes was relatively smaller compared to Motion #2, and the dilation spikes were observed only at shallow depths (AH4 and AH3). This can be attributed to soil densification after Motion #2 as seen from the CPT results (Fig. 9.11c). Consequently, the spectral acceleration and the RRS at the short-period



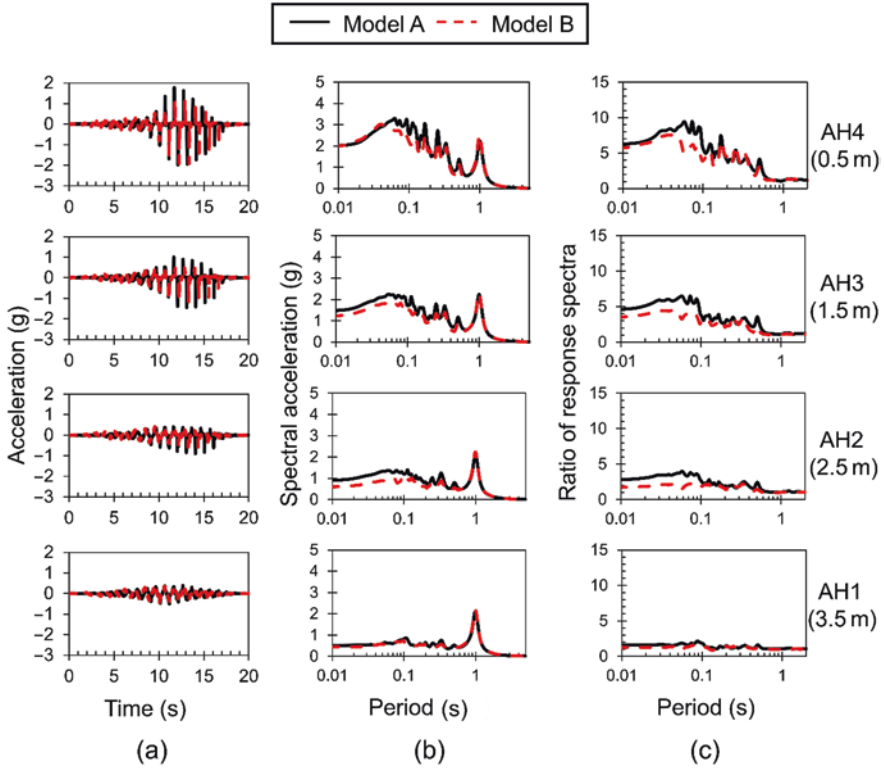


**Fig. 9.12** Acceleration response at different depths for Models A and B during Motion #2: (a) acceleration time history, (b) response spectra, and (c) ratio of response spectra

range in Model A were smaller for Motion #3 (Fig. 9.13b, c) than for Motion #2 (Fig. 9.12b, c).

In Model B, the amplitude of dilation spikes was larger for Motion #3 than for Motion #2. This could be due to larger  $PGA_{eff}$  of Motion #3 (0.371g) than of Motion #2 (0.314g). Also, there was some evidence of loosening in Model B after Motion #2 based on the CPT result (Fig. 9.11c). So, it is reasonable to expect a larger extent of liquefaction during Motion #3, which resulted in bigger dilation spikes. Hence, the spectral acceleration and the RRS at the short-period range were larger during Motion #3 than Motion #2 for Model B.

Overall, the acceleration response of Models A and B is largely similar during Motion #2, while the acceleration response of Model B was larger than that of Model A during Motion #3.

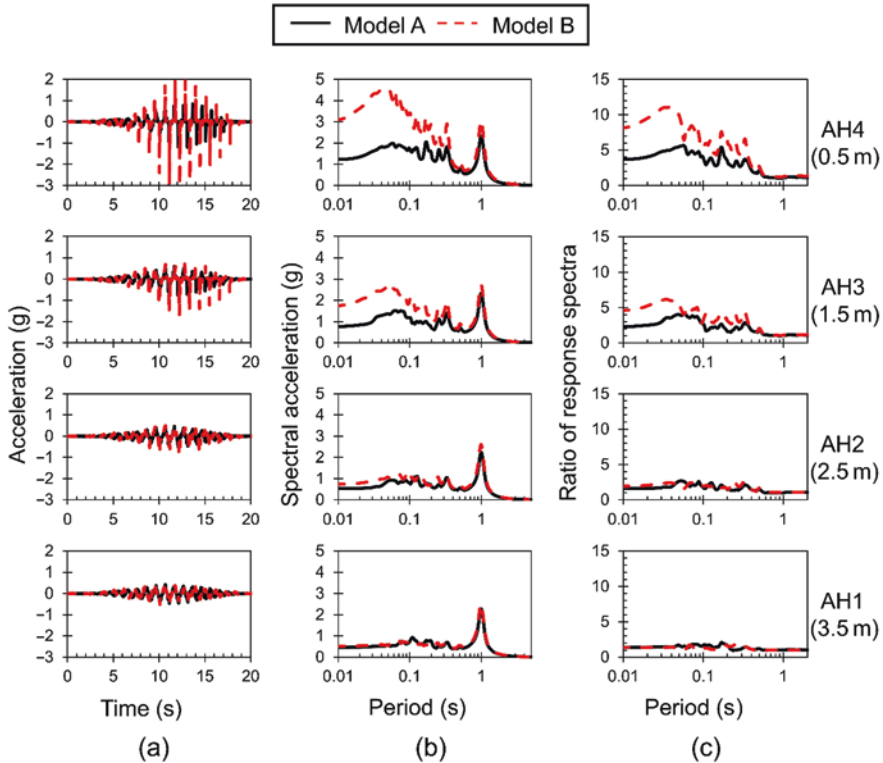


**Fig. 9.13** Acceleration response at different depths for Models A and B during Motion #3: (a) acceleration time history, (b) response spectra, and (c) ratio of response spectra

#### 9.4.4 Excess Pore Pressure Response

The excess pore pressure response during destructive motions in Models A and B was converted to the prototype scale based on scaling factors in Table 9.1. The excess pore water pressure recorded using pore pressure transducers placed at various depths during Motion #2 and Motion #3 is shown in Fig. 9.14. The response of pore pressure transducer P1 installed at 4 m depth in Model A and transducer P2 located at 3 m depth in Model B were not obtained due to malfunctioning of the sensors. The initial vertical effective stresses were approximately 40 kPa, 30 kPa, 20 kPa, and 10 kPa at P1, P2, P3, and P4, respectively. Negatively directed spikes in pore pressure were observed due to soil dilatancy during the destructive motions. On the other hand, the dissipation time of the excess pore pressure was longer in Model B than in Model A. In other words, the experiment, which was performed at lower centrifugal acceleration, required longer dissipation time for the excess pore pressure. These can be attributed to three possibilities: (1) the effect of time duration for consolidation before shaking, (2) small value of shear modulus due to low

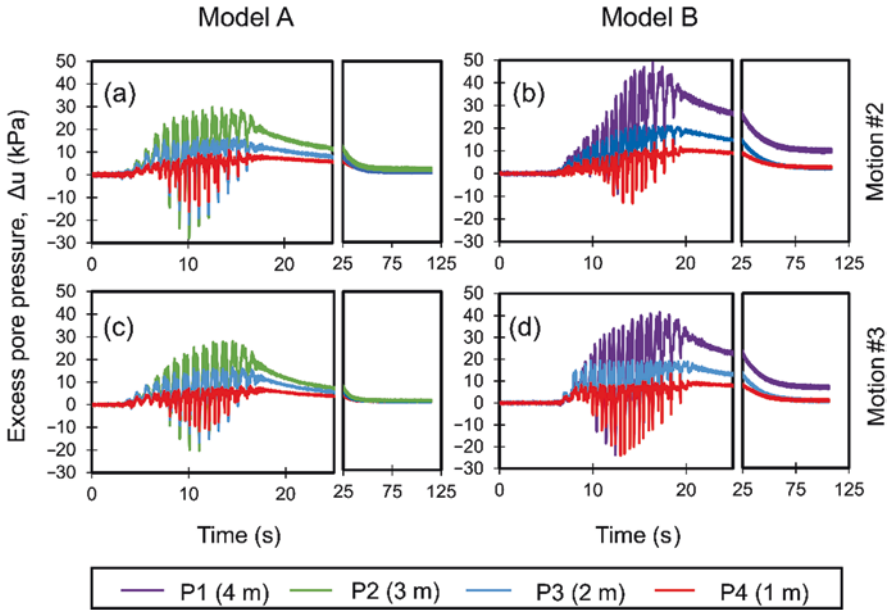


**Fig. 9.14** Excess pore pressure response ( $\Delta u$ ) at different depths: (a)  $\Delta u$  during Motion #2 in Model A, (b)  $\Delta u$  during Motion #2 in Model B, (c)  $\Delta u$  during Motion #3 in Model A, and (d)  $\Delta u$  during Motion #3 in Model B

effective confining stress under low centrifugal acceleration, and (3) possible changes in permeability of the model ground during shaking due to adsorption of the methylcellulose on sand particles (Tobita & Iai, 2011).

Figure 9.15 shows the time history of pore pressure ratio ( $r_u$ ) for each model in order to compare the liquefaction occurrence in Models A and B. The  $r_u$  at a given depth was calculated by dividing the recorded excess pore pressure by the initial vertical effective stress at that depth. The  $r_u$  value equal to 1 is generally considered as an evidence of initial liquefaction. During Motion #2, the  $r_u$  value was close to 1 only at the depth of 1 m (P4) in Model A, while at other depths (P3 and P2), the  $r_u$  value was less than 1. For Model B during Motion #2, the  $r_u$  value reached 1.0 at all depths (P4, P3, and P1). The  $r_u$  value close to 1 at P1 is unlikely due to liquefaction as the dilation spikes were absent in acceleration (AH1) response. This large positive excess pore pressure could be because of an increase in total stress momentarily due to the effect of vertical accelerations, the local dynamic compressive stress around the sensor, and the effect of wire stiffness (Kutter et al., 2020b).

During Motion #3, the  $r_u$  value was less than 1 at all the measured depths for Model A, even though  $PGA_{eff}$  for Motion #3 was slightly bigger. This can be attributed to soil densification after Motion #2, which led to an increase in liquefaction resistance. For Model B, however, the  $r_u$  value reached 1.0 at shallow depths (P4 and P3), and larger dilation spikes were observed than during Motion #2. This could be because of larger  $PGA_{eff}$  for Motion #3 and soil softening following Motion #2. At

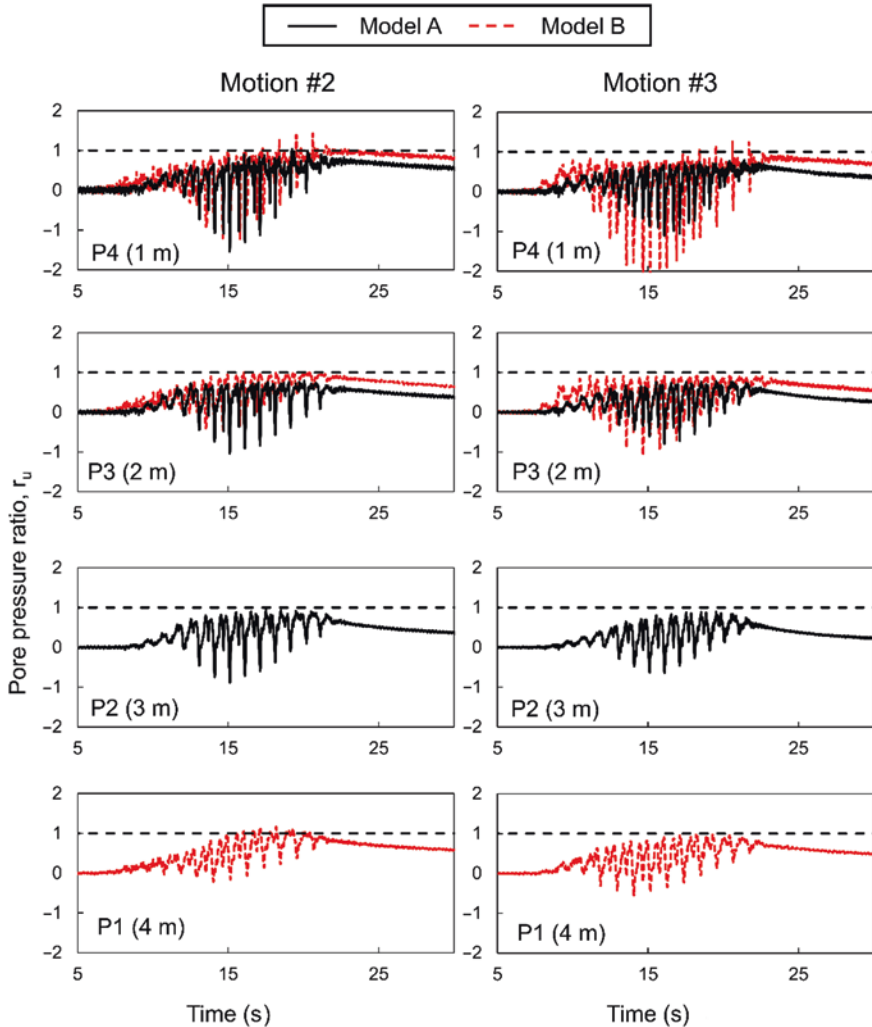


**Fig. 9.15** Pore pressure ratio ( $r_u$ ) for Models A and B during Motion #2 and Motion #3 at different depths

a depth of 4 m (P1), although  $r_u$  value reached 1.0, liquefaction is unlikely for reasons previously mentioned.

Even though  $r_u$  close to 1 was observed at shallow depths in both Models A and B during Motion #2 and Motion #3, it is unlikely that full liquefaction occurred at these depths. Dense soils can generate high  $r_u$  values under severe cyclic loading but still have limited shear potential due to their strong dilation tendency upon continuous shear deformation (Wu et al., 2004). Also, the excess pore pressure dissipated right after the end of shaking, indicating that the extent of liquefaction was fairly limited. This will be clearer upon observing the displacement response of the

sloping ground in Sect. 9.4.6. Hence, it would be reasonable to state that both Models A and B were partially liquefied during Motions #2 and #3.

### 9.4.5 Stress-Strain Response and Effective Stress Path

The stress and strain quantities were converted to the prototype scale based on the corresponding scaling factors for Models A and B (Table 9.1). Figure 9.16 shows the stress-strain curves for Models A and B during Motion #2 and Motion #3 at three different depths. Shear stress time history was calculated at midway point between two accelerometers based on the acceleration response using the equations given in Zeghal et al. (2018). Strain time history was calculated at the midway point between two accelerometers based on the displacement response obtained by the double integration of the acceleration response. During Motion #2, both Models A and B showed similar stress-strain behavior at all the depths. The shear strain was less than 1% with the maximum strain occurring near the surface. During Motion #3, however, the shear strain for Model A is reduced at all the depths as compared with Motion #2. On the other hand, the shear strain for Model B increased at all depths during Motion #3, with strain at the depth of 1 m exceeding 1%. The difference in stress-strain responses during Motion #3 can be attributed to soil densification following Motion #2 for Model A and large amplitude in Motion #3 for Model B. Additionally, stress spikes are observed in both the upslope and downslope directions at all the depths for both models. This could be due to dilative response at shallow depths and a combination of dilative response and soil-container interaction at larger depths (Zeghal et al., 2018).

Figure 9.17 shows the effective stress paths at the depths of 1 and 2 m for Models A and B during Motion #2 and Motion #3. The shear stress ( $\tau$ ) and the vertical effective stress ( $\sigma'_v$ ) were normalized by the initial vertical effective consolidation stress ( $\sigma'_{vc}$ ). The normalized vertical effective stress ( $\sigma'_v / \sigma'_{vc}$ ) reached zero during Motion #2 at 1 m depth in Model A, while it was non-zero in all other cases. This indicates that liquefaction occurred at 1 m depth in Model A during Motion #2, which corroborates with the pore pressure ratio response in Fig. 9.15. In Model B, the  $\sigma'_v / \sigma'_{vc}$  ratio reached zero in all cases, except at the depth of 2 m during Motion #3. On the other hand, the  $\sigma'_v / \sigma'_{vc}$  ratio exceeded 1.0 in all the cases and reached almost 3.0 at 1 m depth during Motion #3 in Model B. This is due to the large negative pore pressure spikes caused by the strong dilative soil response during shaking. As a result, the effective confining stress was much larger during shaking than before shaking. Therefore, the extent of liquefaction was limited even though the  $\sigma'_v / \sigma'_{vc}$  ratio became zero momentarily during shaking.

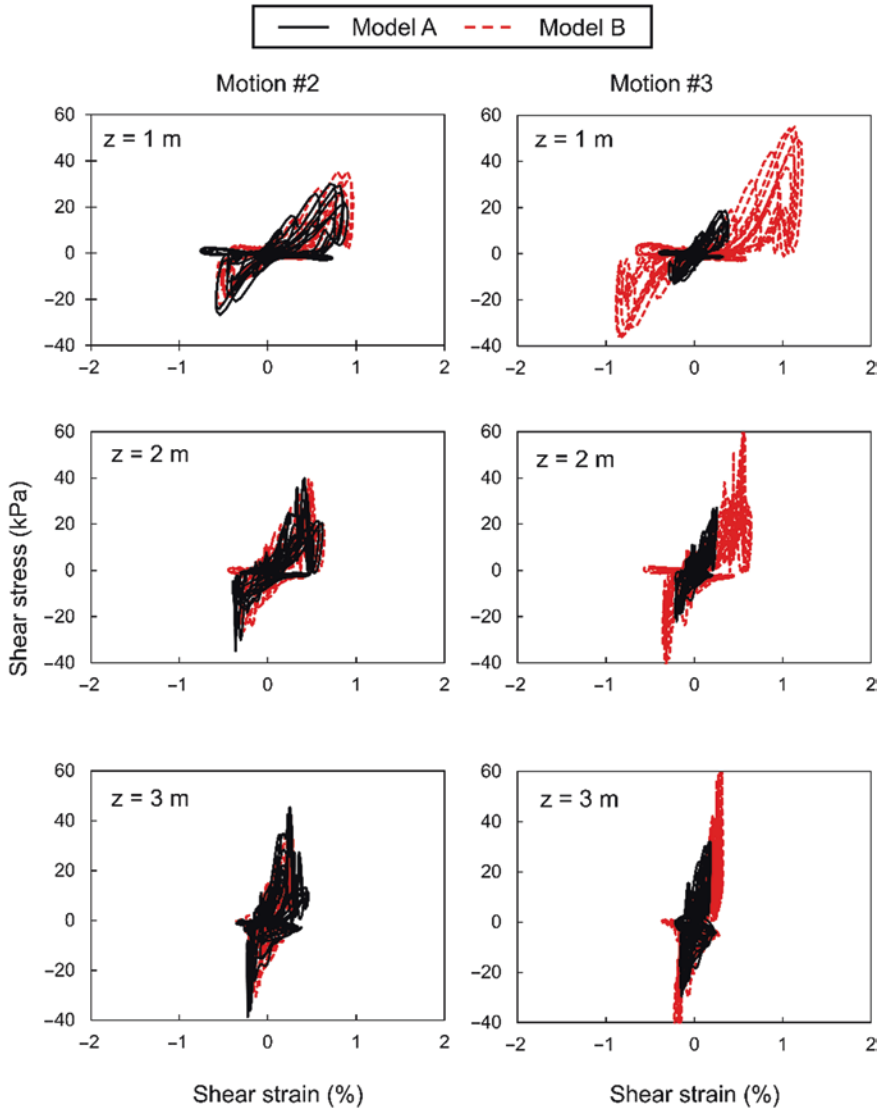


**Fig. 9.16** Stress-strain response of Models A and B during Motion #2 and Motion #3 at three different depths

### 9.4.6 Displacement Response

The prototype displacements for Models A and B are based on scaling factors in Table 9.1. Figure 9.18 shows the schematic of the 18 surface markers and the coordinate system used. The markers were arranged in three longitudinal arrays and six transverse arrays. The coordinates ( $x$ ,  $y$ , and  $z$ ) of the markers were measured before

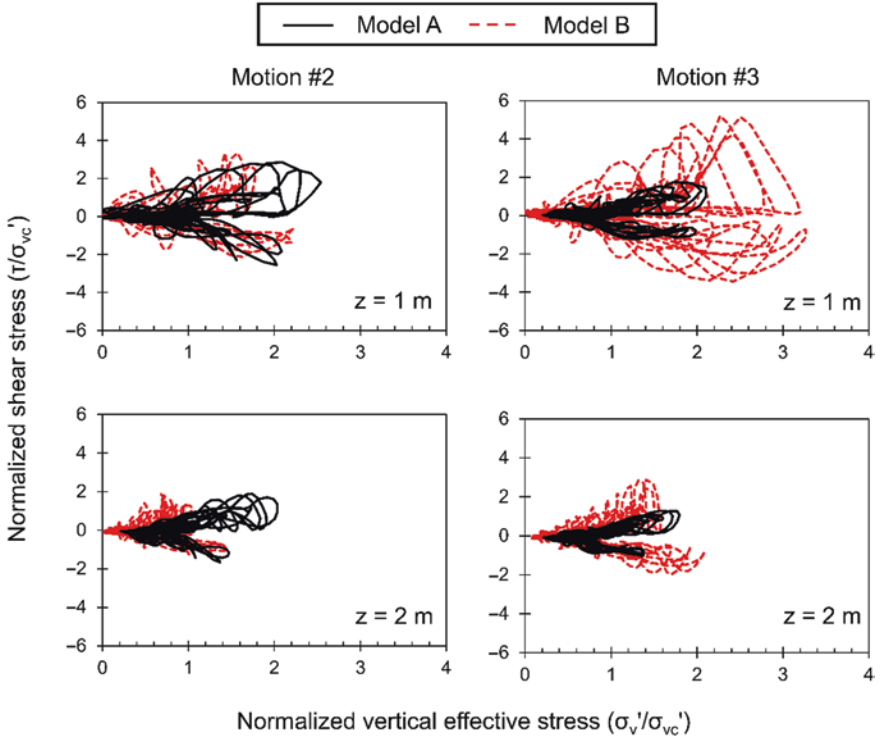


Fig. 9.17 Effective stress paths of Models A and B during Motion #2 and Motion #3

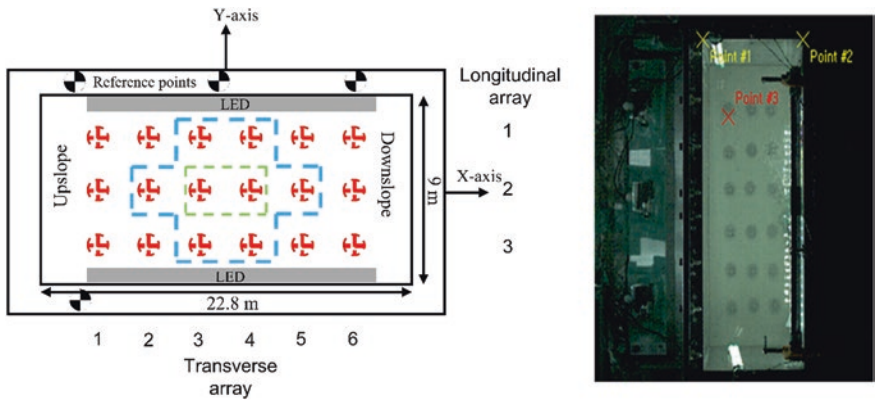
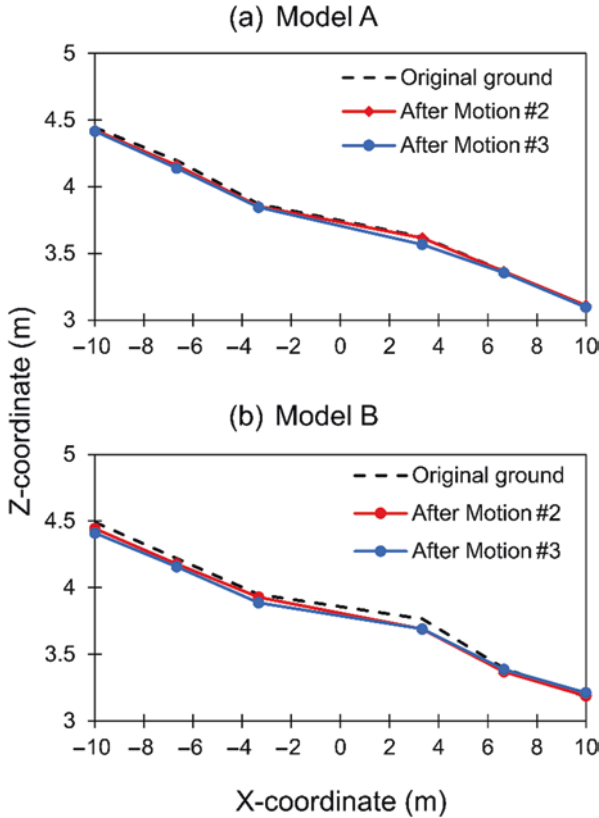


Fig. 9.18 Schematic of the surface markers and coordinate system (18 total markers; 8 markers are included in the blue dotted zone, and 2 central markers are in the green dotted zone). Points #1 and #2 represent the reference points, and Point #3 is the tracking point used in the TEMA software



**Fig. 9.19** Measured vertical settlements along the longitudinal axis of the model after Motion #2 and Motion #3 with the original ground profile: (a) Model A and (b) Model B

Motion #2 (initial position), after Motion #2, and after Motion #3 at 1-g condition. The x-coordinate is in the direction of the shaking, y-coordinate is perpendicular to the shaking direction, and z-coordinate is along the depth of the model. Additionally, horizontal displacements of the markers were recorded during shaking motion using a high-speed camera and tracked using a motion-tracking program, TEMA.

Figure 9.19 shows the variation of vertical displacement of the ground profile along the longitudinal axis after each destructive motion. The vertical displacement is the average displacement of the three markers in each transverse array. Both Models A and B showed minimal settlements with little change in the original ground profile after Motion #2 and Motion #3. The measurement of the central markers (dotted green zone) can be taken as representative as they are less affected by the container boundary. After Motion #2, the average vertical settlements of the two central markers in Models A and B were 26 and 32 mm at the prototype scale, respectively. After Motion #3, the average settlements were about 16 mm and 27 mm for Models A and B, respectively. The settlements were comparatively less



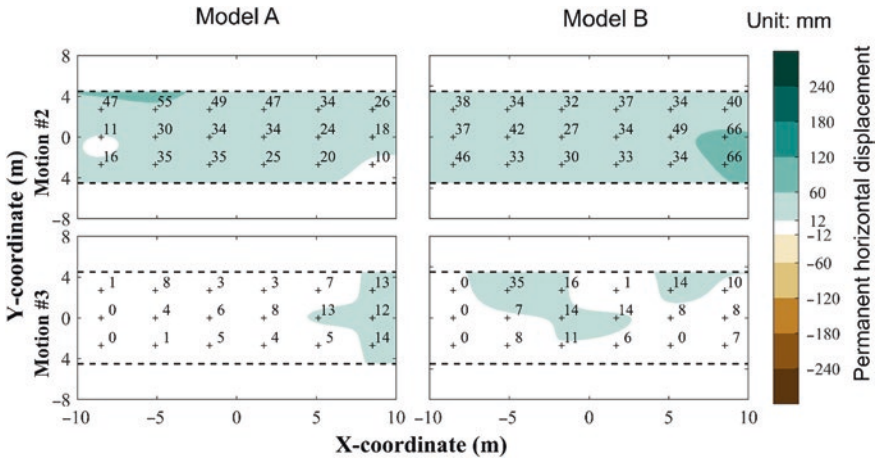


**Fig. 9.20** Contour plots of permanent horizontal displacements (in mm) from tracked marker positions obtained using high-speed camera recording in Model A and Model B during Motion #2 and Motion #3

after Motion #3 than Motion #2 in both the models, and Model B had larger settlements than Model A.

Figure 9.20 shows the comparison of permanent horizontal displacement contours for Models A and B following Motion #2 and Motion #3 in the prototype scale. The values above the markers represent the permanent horizontal displacements in mm calculated based on the time history of tracked marker position during shaking (Fig. 9.21). The contour was created by interpolation between the permanent displacements of the markers. In both the models, the 18 markers moved in the downslope direction following Motion #2, and the average permanent horizontal displacements of the two central markers were 34 and 30.5 mm for Model A and Model B, respectively. Although the permanent displacements in Models A and B were almost same, the transient displacements were much larger in Model B than in Model A. There were oscillations in displacement after the end of motion due to water waves, so the average of displacement values after the end of motion was used to calculate the permanent displacement. In the case of Motion #3, the permanent horizontal displacements in both the models were largely reduced.

### 9.5 Discussion and Conclusions

As a part of LEAP-ASIA-2019, two centrifuge model tests were performed at KAIST to evaluate liquefaction behavior of gently sloping dense grounds (target  $D_r = 85\%$ ) under strong base shaking (target  $PGA_{eff} = 0.3g$ ). The two models, Models A and B, represented the same prototype model but were tested under different centrifugal accelerations to evaluate the generalized scaling law for

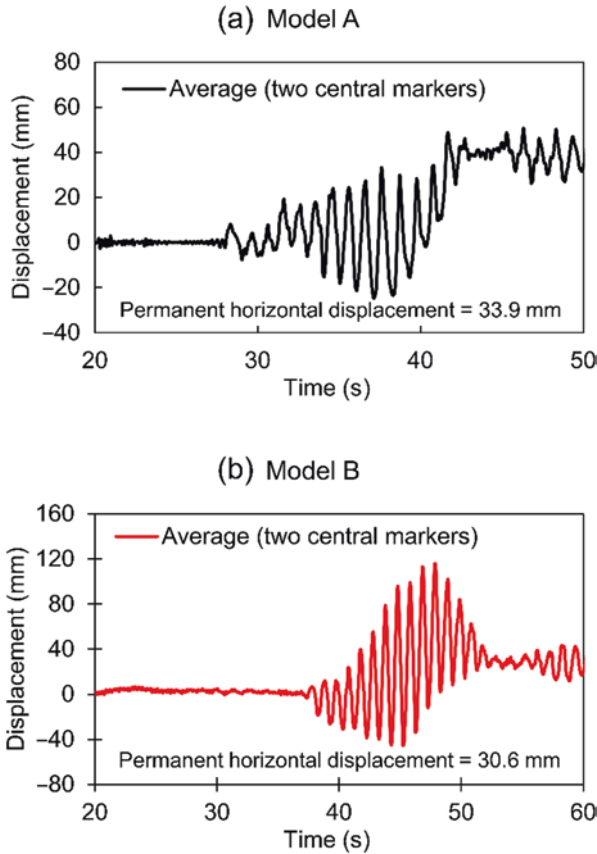


**Fig. 9.21** Horizontal displacement ( $x$ -direction) time histories of two central markers during Motion #2 for Models A and B

simulating liquefaction phenomena in centrifuge tests. Based on the test results, the following can be inferred:

1. Although the same prototype model was simulated using Models A and B, the CPT profiles of the models were similar only at shallow depths ( $<1$  m), while Model A was stiffer than Model B at deeper depths. This shows the effect of larger confining pressure in Model A (40-g centrifugal acceleration) than in Model B (26.7-g centrifugal acceleration), and thus, the generalized scaling law may not be applicable for deeper depths. Another possible reason could be that the generalized scaling law is valid for stress paths up to the peak deviator stress. However, the stress path during CPT testing goes well beyond the peak deviator stress and into the failure zone. Iai et al. (2005) state that we need to use looser material as compared with the prototype when stress path exceeds the peak deviator stress. This can also explain the dissimilarity of CPT results between Models A and B.

2. Upon comparing the CPT results before and after Motion #2, Model A showed ground densification, which is similar to the response of dense model tested at 40-g centrifugal acceleration in LEAP-UCD-2017 at KAIST. However, Model B showed similar  $q_c$  values at shallow depths (<1.5 m) but loosening at deeper depths.
3. Spikes due to dilatant soil behavior were observed in acceleration records at shallow depths (0.5 and 1.5 m) in both Models A and B. The acceleration response of Models A and B was similar during Motion #2, while it differed during Motion #3. This is because of ground disturbance following Motion #2 as well as the large intensity in Motion #3 in Model B.
4. Based on pore pressure ratio ( $r_u$ ), it can be inferred that liquefaction did occur to some extent in dense grounds at shallow depths (1 and 2 m) in both Models A and B. This is in contrast with the response of dense model in LEAP-UCD-2017 at KAIST, where liquefaction did not occur when  $PGA_{\text{eff}}$  of 0.15g was applied. This implies that under sufficiently strong shaking, dense soil deposits can also liquefy but the extent of liquefaction will be limited. Furthermore, the dissipation time of excess pore pressures was longer in Model B than in Model A due to the effect of low confining stress in Model B.
5. Although there was evidence of liquefaction at shallow depths based on  $r_u$  values, significant shear strains were not observed (limited to 1% shear strain) because the soil was initially dense-of-critical (below the critical state line in e-p' plot). Liquefaction of dense-of-critical sand during cyclic loading results in limited strains because the sand exhibits dilatative behavior under subsequent monotonic loading (Idriss & Boulanger, 2008).
6. The stress-strain curves were qualitatively similar for Models A and B during Motion #2, while they were different during Motion #3. This indicates that the generalized scaling law may not be applicable to study stress-strain response of soil after it is disturbed by strong shaking. However, the large shaking intensity of Motion #3 in Model B also caused the observed differences. From the effective stress path, it was observed that the vertical effective stress increased well beyond the initial consolidation stress due to dilatancy causing temporary stiffening of the soil during shaking.
7. The vertical ground settlement profiles were almost the same for Models A and B. Also, there is little difference between settlements after Motion #2 and after Motion #3. Both Models A and B have similar permanent horizontal displacements in the direction of shaking. However, the transient displacements were larger in Model B than in Model A. On the other hand, the permanent horizontal displacements were significantly reduced during Motion #3 as compared to Motion #2 in both the models.

Overall, the response of Models A and B was similar in terms of acceleration, pore pressure response, stress-strain behavior, and ground displacements, except for the CPT profiles. Hence, the generalized scaling law is largely applicable for centrifuge testing of dense model grounds under strong shaking. The large  $PGA_{\text{eff}}$  of Motion #3 and the effect of soil disturbance following Motion #2 caused the observed differences in response between Models A and B during Motion #3. Thus,

in future tests, it is necessary to control shaking intensity of input motion to validate the applicability of the generalized scaling law following a destructive first motion. Further, the scaling factors used for the cone tip resistance and penetration depth should be explored more to validate the generalized scaling law for CPT.

**Acknowledgments** This research was part of the project titled “Development of performance-based seismic design,” funded by the Ministry of Oceans and Fisheries, Korea. The authors also gratefully acknowledge the KREONET service provided by the Korea Institute of Science and Technology Information.

## References

- Arulanandan, K., & Scott, R. F. (Eds.). (1993). *Verification of numerical procedures for the analysis of soil liquefaction problems*. A.A. Balkema.
- Carey, T. J., Gavras, A., & Kutter, B. L. (2020). Comparison of LEAP-UCD-2017 CPT results. In B. L. Kutter, M. T. Manzari, & M. Zeghal (Eds.), *Model tests and numerical simulations of liquefaction and lateral spreading* (pp. 117–129). Springer. [https://doi.org/10.1007/978-3-030-22818-7\\_6](https://doi.org/10.1007/978-3-030-22818-7_6)
- El Ghoraiby, M., Park, H., & Manzari, M. T. (2020). Physical and mechanical properties of Ottawa F65 sand. In B. L. Kutter, M. T. Manzari, & M. Zeghal (Eds.), *Model tests and numerical simulations of liquefaction and lateral spreading* (pp. 45–67). Springer. [https://doi.org/10.1007/978-3-030-22818-7\\_3](https://doi.org/10.1007/978-3-030-22818-7_3)
- Garnier, J., Gaudin, C., Springman, S. M., Culligan, P. J., Goodings, D., Konig, D., et al. (2007). Catalogue of scaling laws and similitude questions in geotechnical centrifuge modelling. *International Journal of Physical Modelling in Geotechnics*, 7(3), 1–23. <https://doi.org/10.1680/ijpmg.2007.070301>
- Iai, S., Tobita, T., & Nakahara, T. (2005). Generalized scaling relations for dynamic centrifuge tests. *Geotechnique*, 55(5), 355–362. <https://doi.org/10.1680/geot.2005.55.5.355>
- Idriss, I. M., & Boulanger, R. W. (2008). *Soil liquefaction during earthquakes*. Earthquake Engineering Research Institute. MNO-12.
- Kim, K., Prezzi, M., Salgado, R., & Lee, W. (2008). Effect of penetration rate on cone penetration resistance in saturated clayey soils. *Journal of Geotechnical and Geoenvironmental Engineering*, 134(8), 1142–1153. [https://doi.org/10.1061/\(ASCE\)1090-0241\(2008\)134:8\(1142\)](https://doi.org/10.1061/(ASCE)1090-0241(2008)134:8(1142))
- Kim, D.-S., Kim, N.-R., Choo, Y.-W., & Cho, G.-C. (2013a). A newly developed state-of-the-art geotechnical centrifuge in Korea. *KSCSE Journal of Civil Engineering*, 17(1), 77–84. <https://doi.org/10.1007/s12205-013-1350-5>
- Kim, D.-S., Lee, S.-H., Choo, Y.-W., & Perdriat, J. (2013b). Self-balanced earthquake simulator on centrifuge and dynamic performance verification. *KSCSE Journal of Civil Engineering*, 17(4), 651–661. <https://doi.org/10.1007/s12205-013-1591-3>
- Kim, S.-N., Ha, J.-G., Lee, M.-G., & Kim, D.-S. (2020). LEAP-UCD-2017 centrifuge test at KAIST. In B. L. Kutter, M. T. Manzari, & M. Zeghal (Eds.), *Model tests and numerical simulations of liquefaction and lateral spreading* (pp. 315–339). Springer. [https://doi.org/10.1007/978-3-030-22818-7\\_16](https://doi.org/10.1007/978-3-030-22818-7_16)
- Kutter, B. L., & Wilson, D. W. (1999). *De-liquefaction shock waves* (pp. 295–310). Proceedings of the seventh US–Japan workshop on earthquake resistant design of lifeline facilities and countermeasures against soil liquefaction.
- Kutter, B. L., Carey, T., Hashimoto, T., Zeghal, M., Abdoun, T., Kokalli, P., Madabhushi, G., Haigh, S., Hung, W.-Y., Lee, C.-J., Iai, S., Tobita, T., Zhou, Y. G., Chen, Y., Manzari, M. T., et al.

- (2018). LEAP-GWU-2015 experiment specifications, results, and comparisons. *Soil Dynamics and Earthquake Engineering*, 113, 616–628. <https://doi.org/10.1016/j.soildyn.2017.05.018>
- Kutter, B. L., Carey, T. J., Zheng, B. L., Gavras, A., Stone, N., Zeghal, M., et al. (2019). Twenty-four centrifuge tests to quantify sensitivity of lateral spreading to Dr and PGA. In *Geotechnical earthquake engineering and soil dynamics V* (pp. 383–393). <https://doi.org/10.1061/9780784481486.040>
- Kutter, B. L., Carey, T. J., Stone, N., Bonab, M. H., Manzari, M. T., Zeghal, M., et al. (2020a). LEAP-UCD-2017 V. 1.01 model specifications. In B. L. Kutter, M. T. Manzari, & M. Zeghal (Eds.), *Model tests and numerical simulations of liquefaction and lateral spreading* (pp. 3–29). Springer. [https://doi.org/10.1007/978-3-030-22818-7\\_1](https://doi.org/10.1007/978-3-030-22818-7_1)
- Kutter, B. L., Carey, T. J., Stone, N., Zheng, B. L., Gavras, A., Manzari, M. T., et al. (2020b). LEAP-UCD-2017 comparison of centrifuge test results. In B. L. Kutter, M. T. Manzari, & M. Zeghal (Eds.), *Model tests and numerical simulations of liquefaction and lateral spreading* (pp. 69–103). Springer. [https://doi.org/10.1007/978-3-030-22818-7\\_4](https://doi.org/10.1007/978-3-030-22818-7_4)
- Okamura, M., & Inoue, T. (2012). Preparation of fully saturated models for liquefaction study. *International Journal of Physical Modelling in Geotechnics*, 12(1), 39–46.
- Tobita, T., & Iai, S. (2011). *Application of the generalized scaling law to liquefiable model ground*. Annuals of Disaster Prevention Research Institute, Kyoto University.
- Ueda, K., & Iai, S. (2018). Numerical predictions for centrifuge model tests of a liquefiable sloping ground using a strain space multiple mechanism model based on the finite strain theory. *Soil Dynamics and Earthquake Engineering*, 113, 771–792. <https://doi.org/10.1016/j.soildyn.2016.11.015>
- Wu J., Kammerer A.M., Riemer M.F., Seed R.B., Pestana J.M. (2004) *Laboratory study of liquefaction triggering criteria*. 13th world conference on earthquake engineering. Vancouver, BC, Canada, Paper No. 2580.
- Zeghal, M., Goswami, N., Kutter, B. L., Manzari, M. T., Abdoun, T., Arduino, P., et al. (2018). Stress-strain response of the LEAP-2015 centrifuge tests and numerical predictions. *Soil Dynamics and Earthquake Engineering*, 11, 804–818. <https://doi.org/10.1016/j.soildyn.2017.10.014>

**Open Access** This chapter is licensed under the terms of the Creative Commons Attribution 4.0 International License (<http://creativecommons.org/licenses/by/4.0/>), which permits use, sharing, adaptation, distribution and reproduction in any medium or format, as long as you give appropriate credit to the original author(s) and the source, provide a link to the Creative Commons license and indicate if changes were made.

The images or other third party material in this chapter are included in the chapter's Creative Commons license, unless indicated otherwise in a credit line to the material. If material is not included in the chapter's Creative Commons license and your intended use is not permitted by statutory regulation or exceeds the permitted use, you will need to obtain permission directly from the copyright holder.

